

Actin bundle architecture and mechanics regulate myosin II force generation

Kimberly L. Weirich,^{1,2,3} Samantha Stam,^{4,5,6} Edwin Munro,^{5,7} and Margaret L. Gardel^{1,2,5,8,*}

¹James Franck Institute, ²Pritzker School of Molecular Engineering; ³Department of Materials Science and Engineering, Clemson University, Clemson, South Carolina; ⁴Biophysical Sciences Graduate Program and ⁵Institute for Biophysical Dynamics, University of Chicago, Chicago, Illinois; ⁶Department of Molecular and Cellular Biology, University of California, Davis, Davis, California; and ⁷Department of Molecular Genetics and Cellular Biology and ⁸Department of Physics, University of Chicago, Chicago, Illinois

ABSTRACT The actin cytoskeleton is a soft, structural material that underlies biological processes such as cell division, motility, and cargo transport. The cross-linked actin filaments self-organize into a myriad of architectures, from disordered meshworks to ordered bundles, which are hypothesized to control the actomyosin force generation that regulates cell migration, shape, and adhesion. Here, we use fluorescence microscopy and simulations to investigate how actin bundle architectures with varying polarity, spacing, and rigidity impact myosin II dynamics and force generation. Microscopy reveals that mixed-polarity bundles formed by rigid cross-linkers support slow, bidirectional myosin II filament motion, punctuated by periods of stalled motion. Simulations reveal that these locations of stalled myosin motion correspond to sustained, high forces in regions of balanced actin filament polarity. By contrast, mixed-polarity bundles formed by compliant, large cross-linkers support fast, bidirectional motion with no traps. Simulations indicate that trap duration is directly related to force magnitude and that the observed increased velocity corresponds to lower forces resulting from both the increased bundle compliance and filament spacing. Our results indicate that the microstructures of actin assemblies regulate the dynamics and magnitude of myosin II forces, highlighting the importance of architecture and mechanics in regulating forces in biological materials.

SIGNIFICANCE The actin cytoskeleton is a biopolymer structural material, with complex and varied architecture, that underlies cell mechanics. Here, we explore how the organization of the actin cytoskeleton impacts the force generation of myosin II filaments. By using simulation and *in vitro* reconstitution, we demonstrate that the actin bundle architecture (interfilament spacing and filament polarity) and cross-linker mechanics impact the duration, direction, and magnitude of myosin-based force generation.

INTRODUCTION

The actin cytoskeleton is an active biopolymer structure that underlies the mechanical behavior of cells, such as their ability to change shape and interact with their surroundings (1). This complex material is constructed from actin filaments (F-actin) that are intricately arranged into various architectures by proteins that cross-link F-actin and control F-actin nucleation and growth (2,3). Cross-linkers bind to two F-actin, promoting the formation of networks and bundles with microstructures and mechanics that vary with cross-linker properties. For example, large, compliant

cross-linkers, such as filamin, favor formation of networks with little angular constraint between filaments that coexist primarily with fine cortical structures (4). By contrast, short, rigid cross-linkers such as α -actinin, fimbrin, and fascin form tightly packed, stiff bundles, capable of bearing loads and acting as cellular tracks, in the cell's interior and protrusions (5,6). Together, these and other proteins build actin architectures that control cell shape, mechanics, and intracellular transport (2,3).

Embedded myosin motor proteins transform passively cross-linked actin architectures into active materials (7). Myosin motors undergo a mechanochemical cycle, during which ATP hydrolysis results in the motor binding to F-actin, exerting a force on the F-actin, and detaching from F-actin to restart the cycle. Myosin force generation was originally investigated in striated muscle, where actomyosin assemblies have well-defined sarcomeric organization (8). In

Submitted July 20, 2020, and accepted for publication March 12, 2021.

*Correspondence: gardel@uchicago.edu

Kimberly L. Weirich and Samantha Stam contributed equally to this work.

Editor: Alexander Dunn.

<https://doi.org/10.1016/j.bpj.2021.03.026>

© 2021 Biophysical Society.



sarcomeres, collections of ~500 myosin II motor heads polymerize into a bipolar filament, where the heads each exert step-like forces in a directed fashion toward the barbed end of F-actin. The microstructure of a sarcomere unit, in which anchored F-actin is arranged with opposing polarity, is key to the collective myosin II forces resulting in a net contractile force (9). Myosin II force generation is also critical in non-muscle cells, where F-actin assemblies lack well-defined sarcomeric order but instead have disordered polarity, polydisperse filament length, and various angular orientations and mechanical anchorings. The complex microstructures in nonmuscle cells are likely to spatially regulate the activity of myosins and other proteins. For example, F-actin spacing in bundles influences protein binding and localization, whereas F-actin polarity and angle can direct transport (10–13). Unlike in sarcomeres, where F-actin arranged with opposing polarity supports contractile force generation, in filopodia F-actin are arranged with the same polarity, which may facilitate transport into cellular protrusions by transport-oriented myosin isoforms such as myosin X (2,14). However, despite evidence that cytoskeletal architecture can impact protein localization and cargo motility generated by transport motor proteins (10,13,15–17) and that network architecture is critical to myosin-driven contractility (18–20), the role of F-actin architecture in myosin II force generation remains an open question.

Here, we investigate the impact of F-actin architecture on myosin II-based forces in model actomyosin experiments reconstituted from purified proteins and through complementary agent-based simulations. Through fluorescence microscopy, we find that isolated filaments of skeletal muscle myosin II (myosin) move throughout space on cross-linked F-actin networks but have bidirectional motion confined to micron-sized regions on F-actin bundles. To understand the origins of the confinement, we construct actin bundle architectures *in vitro* and *in silico* with different filament polarity and spacing. On mixed-polarity bundles with small interfilament spacing, we find that myosin moves bidirectionally, at speeds nearly an order of magnitude below the gliding velocity, punctuated by periods in which motors are nearly stalled. By contrast, on mixed-polarity bundles formed by cross-linkers that support large interfilament spacing and angular flexibility, myosin moves bidirectionally without stalling. Intriguingly, increasing the amount of cross-linking in these spaced, compliant bundles causes myosin motion to be similar to smaller-spaced, rigid bundles, with regions of confined, stalled motion. The simulations show that although the myosin is robustly confined to traps in balanced polarity regions with small interfilament spacing, the relationship between the force myosin exerts on a F-actin bundle and the bundle microstructure is complex. Through simulations, we can decouple the effects of cross-linker spacing and compliance. To capture the dynamics that we see in bundles experimentally constructed with large, compliant cross-linkers, it is necessary that cross-linkers impose large spacing, while

low spring constants enhance the bidirectional motion. Our results show that myosin motion and forces are sensitive to bundle architecture, indicating that cytoskeletal microstructure and mechanics may be an important regulator of cellular force production.

MATERIALS AND METHODS

Experimental assay

Protein preparation

Rabbit skeletal muscle is purified from acetone powder (Pel-Freez Biologicals, Rogers, AR) as described in (21). Actin is visualized by incorporating ~25% actin monomers that were labeled with the fluorophore tetramethylrhodamine-6-maleimide (Life Technologies, Carlsbad, CA). F-actin polymerization buffer is composed of 10 mM imidazole, 50 mM KCl, 0.2 mM EGTA (pH 7.5), and 300 μ M ATP. Cross-linking proteins human fascin (22) and *Schizosaccharomyces pombe* fimbrin (23) are prepared using established protocols from D. Kovar lab (University of Chicago). Human α -actinin is purified from insect cells using established protocol (24). Filamin is purified from chicken gizzard using a protocol modified from (25). Skeletal muscle myosin II is purified from chicken according to standard protocol (26) and fluorescently labeled with Alexa 647 (Life Technologies), as described in (27). Myosin II filaments are pre-formed by adding monomeric myosin II to buffer with the same composition as the final sample (F-actin polymerization buffer plus 0.3 wt% 15 centipoise methylcellulose (Sigma-Aldrich, St. Louis, MO), oxygen scavenging system (50 μ M glucose, 0.5 vol% β -mercaptoethanol, glucose oxidase (Calbiochem, San Diego, CA), catalase (Sigma-Aldrich)), and excess ATP) to a final concentration of 20 nM myosin and incubating for 10 min.

Experimental assay

The sample chamber is a channel formed by a thin (2 mm) Teflon gasket (McMaster-Carr, Elmhurst, IL) pressed against a borosilicate coverslip (Thermo Fisher Scientific, Waltham, MA). Glass and Teflon are rinsed with pure ethanol (200 proof; Decon Labs, King of Prussia, PA), then pure water (milliQ), and pure ethanol again before drying with a stream of air. Glass is then exposed to ultraviolet-ozone (UVO cleaner; Jelight, Irvine, CA) for at least 15 min before immediately assembling the sample chamber and filling with vesicle buffer (140 mM NaCl, 8.5 mM Na₂HPO₄, 1.5 mM NaH₂PO₄ (pH 7.5)). The glass surface is passivated against protein adhesion by a supported lipid bilayer. After drying films of 1,2-dioleoyl-*sn*-glycero-3-phosphocholine (Avanti Polar Lipids, Alabaster, AL) under filtered nitrogen gas and resuspending in vesicle buffer, the lipid suspension is extruded (200 and 50 nm pore membranes, Liposofast extruder; Avestin, Ottawa, Canada) to form unilamellar vesicles. Incubating the sample chamber with 1 mM vesicle suspension results in a complete supported lipid bilayer in <5 min. The sample solution is then exchanged by rinsing 15 \times with F-actin polymerization buffer. A final exchange is done with sample buffer containing 4 mM ATP. After 30 min of polymerization, cross-linker protein is added to a concentration between 0.1 and 10 mol% of the acting monomer concentration to bundle the F-actin. After 30 min, the bundled F-actin network reaches a steady state, and myosin II filaments are added to the sample to a final concentration of 3.8 pM myosin. The final ATP concentration is 2.3 mM.

The samples are imaged with an inverted microscope (Nikon Eclipse Ti-PFS; Nikon, Tokyo, Japan) equipped with a spinning disk confocal head (CSUX; Yokogawa, Tokyo, Japan), 561 and 647 nm laser lines, 60 \times /1.49 NA oil immersion objective (Carl Zeiss, Oberkochen, Germany), and a CCD camera (Coolsnap HQ2; Teledyne Photometrics, Tucson, AZ). Images, collected at 1.5 s intervals, began ~10 min after myosin is added to sample.

Image analysis

The frame-to-frame velocity of myosin II puncta is obtained through using fluorescent speckle microscopy software (28). Thresholded images of networks are obtained via ImageJ. Using the bundle threshold as a mask via MATLAB (The MathWorks, Natick, MA), velocities are selected that correspond to motors localized to bundles. Maximal intensity projections are obtained through the built-in Max Projection function of ImageJ, collapsing 300 s of data, collected at 1.5 s intervals, onto a single plane. Regions of myosin localization along bundles appear as bright linear regions in the maximal intensity projection. A line is drawn along the bundle that extends through these bright regions identified in the maximal intensity projection. Then, the intensity along the line is plotted vertically through each time point in the image sequence using the built-in ImageJ function, Reslice.

Simulation methods

Agent-based simulations were conducted using software we have previously described (29) that has been benchmarked to reproduce the gliding speed and force-velocity curves of myosin II using relevant experimentally determined single-molecule parameters. Below, we describe these methods in brief; the values of all parameters are given in Table 1.

F-Actin is represented as a rigid rod, actin cross-linkers are represented as flexible springs, and myosin filaments are represented as rigid rods with extruding elastic elements capped by F-actin binding sites that represent the motor domains. Each of these elastic elements has a spring constant describing resistance to motion parallel to an F-actin, $K_{x\text{-bridge, par}}$ as well as a weaker spring constant for perpendicular motion, $K_{x\text{-bridge, perp}}$ that prevents bound F-actin from drifting. The actin bundle structure in Fig. 3, B and C is one-dimensional. F-actin are directly placed on top of one another, and there is no excluded volume. In all other simulations, actin bundles are two-dimensional, with F-actin that are initially parallel and placed at positions with spacing s . The polarity of the actin alternates between adjacent filaments for two-dimensional bundles. In all simulations, 100 cross-linkers are placed at random locations in the bundle with an initial distance between their bound sites on the F-actin determined by $s_{\text{binding site}}$. F-actin cross-linkers are bound at the beginning of the simulations and remain bound throughout the simulation.

A single myosin filament with an N_{heads} on each end with a spacing of s_{motor} is added to the bundle. Motor domains are initially unbound at the beginning of a simulation and then stochastically bind and unbind via the

Gillespie algorithm (37) with rates k_{on} and $k_{\text{off}}(F)$, respectively. The unbinding rate $k_{\text{off}}(F)$ follows the experimentally determined form (32):

$$k_{\text{off}}(F) = k_{\text{off}}(0) \left[\alpha_{\text{catch}} \exp(-Fx_{\text{catch}} / k_B T) + \alpha_{\text{slip}} \exp(Fx_{\text{slip}} / k_B T) \right], \quad (1)$$

where the force F is positive for a load resisting the myosin step, k_B is Boltzmann's constant, T is temperature, x_{catch} and x_{slip} are characteristic bond lengths, and α_{catch} and α_{slip} are constant prefactors. As a result of this form, the myosin bonds are catch bonds in which opposing forces slow the unbinding rate and assisting forces increase the unbinding rate provided that the force is below a threshold magnitude. Above this magnitude, the bond is a conventional slip bond where opposing forces increase unbinding.

Myosin heads are constrained to bind only to actin filaments with barbed ends on the same side. Binding of a myosin motor domain is permitted if an actin monomer is at least a distance of 25 nm (motor head diameter, d_{motor} plus stalk length, d_{stalk}) from the base of the motor attachment point on the myosin filament. Every unbound myosin motor assigns each actin filament a binding probability given by a Gaussian with a peak probability of k_{on} and a half-width of 10 nm that decreases with distance from the myosin head to the nearest actin monomer. Stochastic binding proceeds using the Gillespie algorithm (37). If a given actin filament gets randomly chosen by this process, the myosin binds to the monomer it is closest to.

The myosin step is a result of the elastic motor domains binding actin in a prestrained state where the elastic element parallel to the actin filament is stretched by a distance d_{step} . Subsequent relaxation of the elastic element causes the relative motion between the F-actin and myosin filaments. Motion of each filament proceeds by numerically solving its equation of motion:

$$0 = -\gamma \dot{x} + F_p + F_{\text{ext}} + \sqrt{2\gamma k_B T} R(t), \quad (2)$$

where γ is the drag coefficient in a medium with a viscosity of $0.1 \text{ N} \cdot \text{s}/\text{m}^2$, F_p is the force exerted by bound proteins, F_{ext} is an external load that is zero for myosin filaments and is imposed by anchoring springs for F-actin, x is the spatial coordinate, and $R(t)$ is a random number drawn from a Gaussian distribution to yield the thermal force in final term of Eq. 2. The simulation proceeds by calculating the instantaneous forces exerted on individual objects during a discrete time step (10^{-5} s). For each object, these forces are entered into Eq. 2, which is solved for \dot{x} . An object then moves according to the value of this velocity, and the process is repeated every time step. Each

TABLE 1 Parameters used in simulation

Name	Description	Value	Reference
N_{heads}	number of heads on one side of myosin filament	variable; 2–300	(47)
k_{on}	binding rate	10 s^{-1}	(30)
$k_{\text{off}}(0)$	unloaded unbinding rate	500 s^{-1}	(31)
α_{catch}	see Eq. 1	0.92	(32)
α_{slip}	see Eq. 1	0.08	(32)
x_{catch}	see Eq. 1	2.5 nm	(32)
x_{slip}	see Eq. 1	0.4 nm	(32)
$k_{\text{off}}(F)$	force-dependent unbinding rate	see Eq. 1	(32)
d_{step}	step size	5.5 nm	(33)
$K_{x\text{-bridge, par}}$	myosin cross-bridge stiffness parallel to F-actin	0.7 pN/nm	(33)
$K_{x\text{-bridge, perp}}$	myosin cross-bridge stiffness perpendicular to F-actin	0.2 pN/nm	N/A
k	stiffness of F-actin cross-linkers and springs that anchor F-actin	variable; 0.001–10 pN/nm	(34,35)
$s_{\text{binding site}}$	spacing of binding sites for motors or cross-linkers along F-actin	2.7 nm	(29)
s_{motor}	spacing between myosin motors	5 nm	(29)
s	spacing between F-actin	variable; 10–200 nm	(6,44,48,49)
d_{motor}	diameter of myosin motor head	10 nm	(36)
d_{stalk}	length of stalk connecting motor head to myosin filament	15 nm	(36)

N/A, not applicable.

object calculates its equation of motion independently, and F_p is the sum of forces on an object coming from attachments to other proteins.

Data analysis

Fitting of force-velocity curves to the hyperbolic Hill equation (38) was done by using the stall force and maximal gliding velocity of the simulated myosin filament (29) and taking the coefficient of shortening heat to be a fitting parameter. Mean-square displacement (MSD) curves were fitted to the following equation:

$$MSD = D^* \Delta t^\alpha,$$

where $D^* \propto D$, the generalized diffusion coefficient; Δt is the time delay; and α is the scaling exponent. All curve fitting was done using the `NonLinearModel.fit` function in MATLAB.

RESULTS

To investigate the impact of actin architecture on myosin II dynamics and force generation, we use confocal microscopy to image single skeletal muscle myosin II filaments on F-actin assemblies reconstituted in vitro. We polymerize F-actin (2.6 μM monomeric actin), crowd it into a thin layer near the surface of a passivated coverslip with a depletion agent, and cross-link the F-actin with the physiological cross-linker, α -actinin. At low concentration (0.1 mol%), α -actinin cross-links the F-actin into networks; as the α -actinin concentration increases to 10 mol%, F-actin form bundles within the network (Fig. 1, A and B). Once the network forms, we add preformed myosin II filaments, which appear as isolated puncta (Fig. 1 B, white puncta). The number density of myosin puncta on the network is sufficiently low ($\sim 5 \times 10^{-3}$ myosin puncta/ μm^2) that they do not generate enough force to deform the network (39,40).

On sparsely cross-linked (0.1 mol%) F-actin, myosin II puncta are highly motile. Summing the myosin intensity over a period of 5 min and projecting on a single image reveal regions of extended tracks sparsely distributed over a large area (Fig. 1, Ci and Di). By contrast, in the corresponding projections on F-actin bundles cross-linked by 1–10 mol% α -actinin, myosin puncta localize to dense, micron-sized linear regions along individual F-actin bundles (Fig. 1, Cii and Dii, 1 mol% and Ciii and Diii, 10 mol%). To quantify differences in myosin speed, we tracked single myosin puncta (Fig. 1 E). The probability distribution reveals that that on α -actinin cross-linked bundles, myosin have instantaneous speeds of <50 nm/s $\sim 80\%$ of the time (Fig. 1 F, solid black circles). By contrast, on the cross-linked actin networks, myosin have speeds >50 nm/s 60% of the time (Fig. 1 F, open gray circles), indicating that the amount of α -actinin-mediated bundling influences myosin puncta speed.

F-actin polarity regulates myosin II filament velocity on rigid bundles

To elucidate the marked influence F-actin bundling has on myosin dynamics, we construct different F-actin bundle architectures from physiological cross-linkers. The most basic F-actin bundle architecture is a unipolar bundle in which the F-actin are all oriented in the same direction (Fig. 2 A). To construct bundles with this architecture, we cross-link F-actin with fascin, a globular protein that mediates unipolar F-actin bundle formation with interfilament spacing <10 nm (Fig. 2 Bi; (6,10)). Intensity projections over 5 min reveal myosin puncta at regular intervals along the fascin cross-linked bundle, indicating uniform myosin speed (Fig. 2 Ci). From a kymograph obtained along a bundle, we find that myosin puncta move persistently in one direction with a constant velocity (Fig. 2 Di, left). Over 104 tracks, we find that $\sim 90\%$ of myosin move persistently and $\sim 100\%$ unidirectionally (Fig. 2, E and F, blue), consistent with previous reports of single motor dynamics on unipolar bundles (16,41). Quantifying the frame-to-frame instantaneous velocity indicates myosin has an average velocity of ~ 2.5 $\mu\text{m/s}$ on fascin bundles (Fig. 2 G, solid blue circles), consistent with the unloaded velocity of skeletal muscle myosin II reported from gliding filament assays of single F-actin (42,43). This indicates that unipolar bundles do not impact the gliding of myosin II filaments, suggesting that myosin puncta exert low forces on the unipolar bundles.

We next constructed bundles from cross-linkers that do not constrain the F-actin polarity within bundles. To change polarity without influencing bundle mechanics, we used fimbrin (5 mol%, Fig. 2, Aii and Bii), a cross-linker that maintains F-actin spacing similar to fascin (10,44). Projections of the myosin intensity over 5 min appear as dense linear tracks along the bundle with limited extent (Fig. 2 Cii, white), indicating myosin II puncta have slow velocities and are confined to isolated regions on mixed-polarity bundles. Kymographs of the myosin trajectory along the bundle reveal diagonal lines, indicating periods of directed motion, punctuated by vertical lines indicating periods of immotility or traps (Fig. 2 Dii). From inspecting 153 tracks, we find that $\sim 40\%$ of myosin are trapped, whereas $\sim 45\%$ of myosin move intermittently and only $\sim 15\%$ move continuously (Fig. 2 F, black). From the 85 independent tracks of motile myosin, we find both positively and negatively sloped lines in $\sim 80\%$ of the tracks (Fig. 2 E, black), indicating bidirectional motion along the bundle, consistent with reports of single motor dynamics on mixed-polarity bundles (16). Additionally, the kymograph lines have larger slopes on mixed-polarity bundles than on the unipolar bundles, indicating slower instantaneous velocities (Fig. 2 D). Quantifying the instantaneous velocity reveals that motile fractions of myosin puncta have speeds of ~ 300 nm/s, nearly an order of magnitude slower than those observed on unipolar bundles (Fig. 2 G, open black circles).

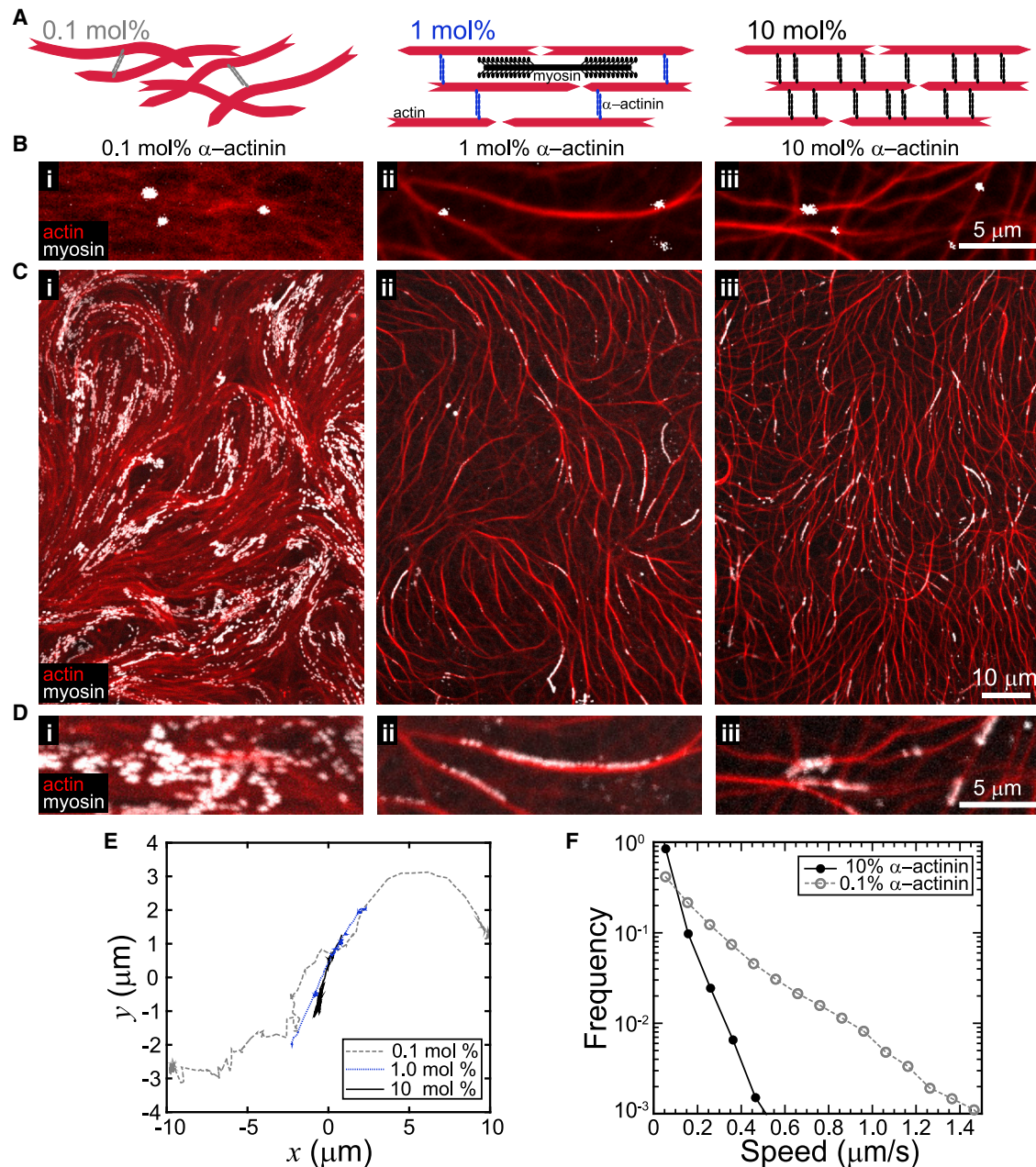


FIGURE 1 F-actin network architecture regulates myosin II motility. (A) Cross-linker constructs F-actin into architectures such as networks and bundles. (B) Fluorescence microscope images of F-actin (red) cross-linked by α -actinin with sparse myosin II filaments (white puncta). Network architecture is modulated by α -actinin concentration; networks of F-actin (left), networks with slight bundling (middle), and networks of bundles (right) form by cross-linking F-actin with 0.1 mol%, 1 mol%, and 10 mol% α -actinin, respectively. Isolated myosin II filaments (white puncta) localize to the networks. (C) Maximal intensity projection over 300 s of myosin II puncta dynamics on networks. (D) Zoomed-in region of maximal intensity projection of myosin II on F-actin architectures in (B). (E) Representative trajectories of myosin II on networks with increasing amounts of α -actinin, transitioning between networks (0.1 mol %) and networks of bundles (1 mol%, 10 mol%). Motors on sparsely cross-linked networks explore more space, whereas motors on higher cross-linked bundled networks are restricted to linear movement along a particular bundle. (F) Distribution of myosin II instantaneous velocities, indicating that motor speed is reduced on higher cross-linked networks. To see this figure in color, go online.

Traps are regions of balanced polarity, where myosin has sustained high forces

Decreased myosin puncta speed and trapped periods on mixed-polarity bundles could result from multiple physical mechanisms, such as direction switching, tug-of-war, or ki-

netic trapping (16,40). Using a computational model, we investigate the microscopic mechanisms by which F-actin bundle architecture impacts myosin filament dynamics in silico (29). In each agent-based simulation, we place a bipolar myosin filament in the center of a F-actin bundle (Fig. 3A). The bipolar myosin filament is composed of two parallel

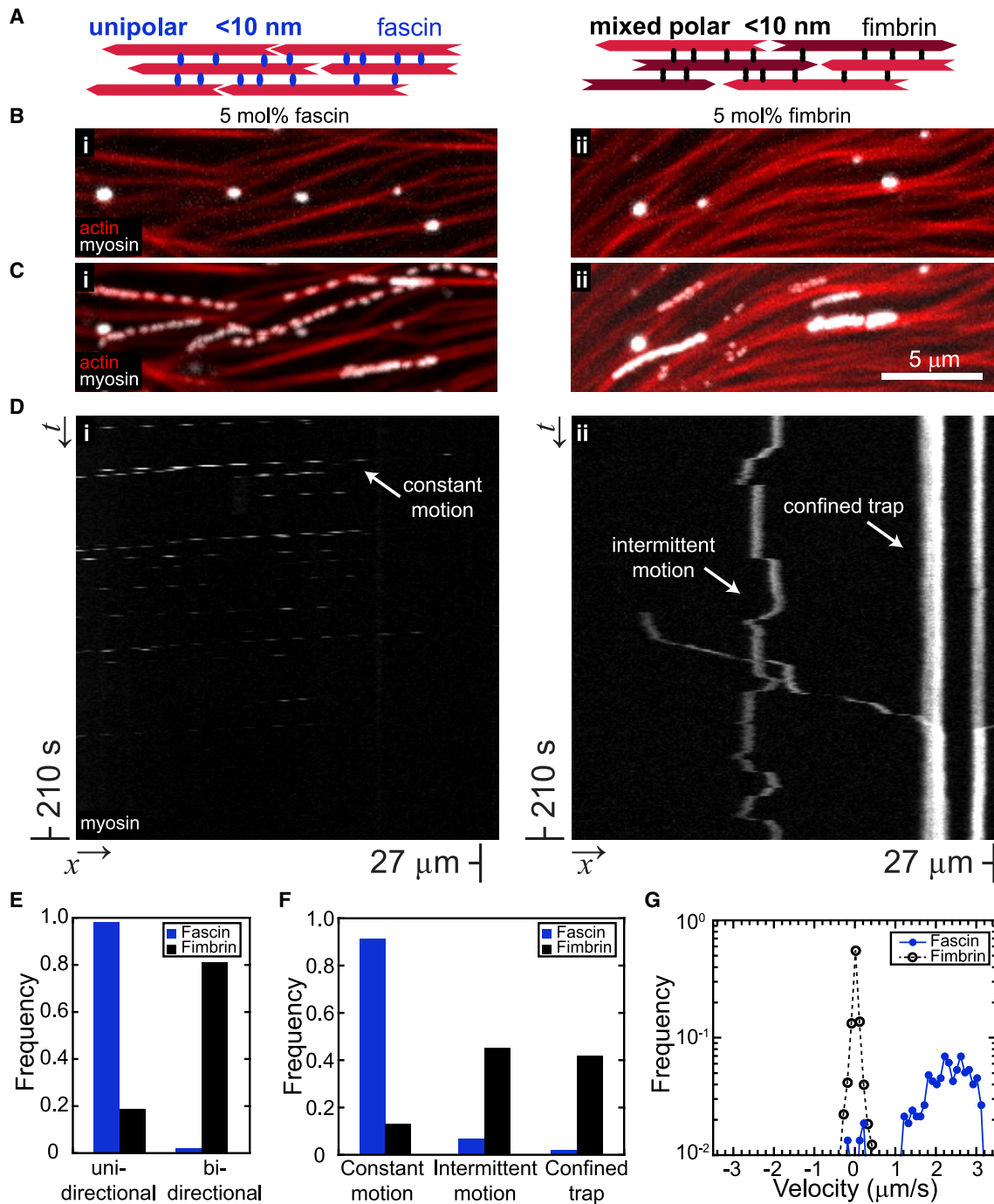


FIGURE 2 F-actin bundle polarity regulates myosin II dynamics. (A) Cartoon of tight unipolar bundles formed by fascin, in which F-actin are oriented in the same direction (*left*) and mixed-polarity bundles formed by fimbrin, in which F-actin are oriented in both directions (*right*). (B) F-actin bundles (*red*) cross-linked by 5 mol% of the unipolar cross-linker, fascin (*left*), and the mixed-polarity cross-linker, fimbrin (*right*), with isolated myosin II filaments (*white puncta*). (C) Maximal projection of myosin II (*white*) over 5 min on fascin-bundled F-actin (*left, red*) and fimbrin-bundled F-actin (*right, red*). On fascin-bundled F-actin, myosin appears as separated puncta distributed evenly along the bundles, whereas on fimbrin-bundled F-actin, myosin localizes to dense regions of a few microns. (D) Kymograph of myosin II motor on fascin-bundled (*left*) and fimbrin-bundled F-actin (*right*). Myosin move along parallel diagonal lines, indicating myosin that bind to the bundle at different times and move with a similar constant velocity in one direction along the bundle. In contrast, on fimbrin bundles, myosin undergo periods of motion, with both positive and negative slopes indicating bidirectional motion, interspersed with periods of traps (*vertical lines*). (E) Proportion of myosin moving along a bundle in one or two directions in a single processive run. (F) Summary of the frequency of myosin dynamics—intermittent motion and pauses, constant motion, or sustained pauses—from kymographs represented in (D). Each myosin (5 mol% fascin: 104 and 5 mol% fimbrin: 153 myosin) was observed over 300 s periods along a bundle section. (G) Myosin II velocity distribution on fascin bundles (*left*) indicates unidirectional motion with magnitude similar to unloaded gliding speed. In contrast, myosin II velocity distribution on fimbrin bundles (*right*) is symmetric about zero, indicating bidirectional motion, with a peak at zero, indicating strong trapping. To see this figure in color, go online.

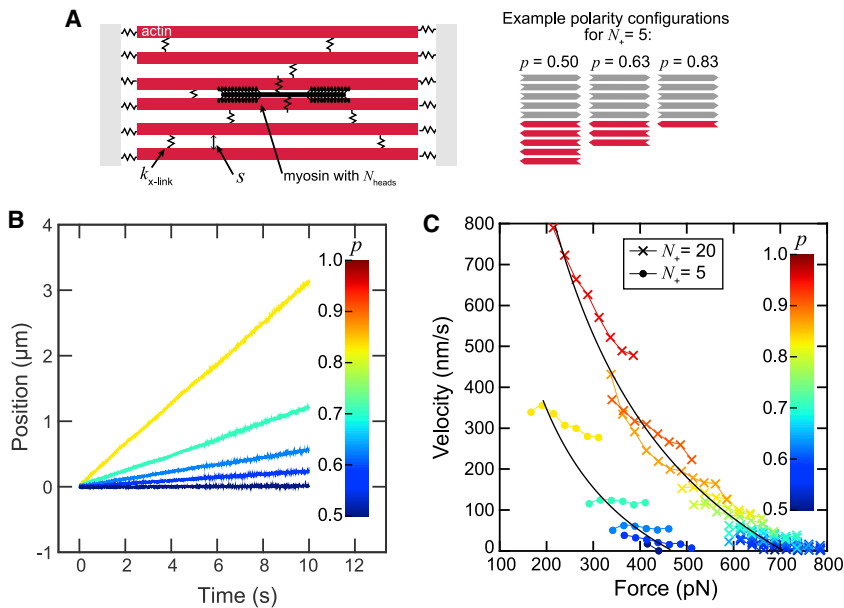


FIGURE 3 Regions of mixed polarity trap myosin filaments and maximize force output. (A) Simulation schematic. A myosin filament is positioned at the center of an actin bundle, where actin filaments are oriented with barbed ends to the left or right. The highlighted myosin motor domains each are represented by springs that bind and unbind to F-actin with rates k_{on} and k_{off} , respectively. The spring stretches upon binding, then relaxes, resulting in the myosin moving relative to the F-actin. The F-actin are attached to springs with stiffness k anchoring them in place and springs with stiffness k representing interfilament cross-links. (B) Trajectories of myosin filaments ($k = 5$ pN/nm) with varying actin polarity. The number of F-actin with barbed ends to the right, N_+ , is held constant at 5 while N_- is varied between 1 and 5. At larger values of N_- indicated by darker blue, myosin filaments are increasingly trapped in place and undergo small changes in direction. (C) Force-velocity curves in which the instantaneous velocity of the myosin filament is plotted against the instantaneous force stored in the myosin springs. Each reported point represents the average force, binned in increments of 25 pN. Blue curves include

simulations in which N_+ is held constant and N_- is varied from 1 to 5, with darker shades indicating larger numbers. Red curves show equivalent data in which N_+ is equal to 20 and N_- is varied from 1 to 20. The value of N_{heads} is 250 for all curves. Each curve contains data from 20 independent 10 s simulations. To see this figure in color, go online.

arrays, connected by a central region. The individual motors are represented by a simple form of the swinging cross-bridge model and benchmarked to skeletal muscle myosin (29). The number of myosin motor domains, N_{heads} , is equal on each end of the myosin filament. We construct bundles by anchoring individual F-actin via springs of stiffness, k , attached at both ends. Cross-linkers are represented by springs, which also have stiffness, k , and rest length, s , that sets the F-actin spacing in a bundle. The polarity, p , of a bundle is defined as the proportion of the F-actin oriented with barbed ends in the positive direction, $N_+/(N_+ + N_-)$. To vary p , we hold the number of F-actin with barbed ends in the positive direction, N_+ , constant while varying the number of F-actin with barbed ends in the opposing direction, N_- .

We systematically vary the polarity of a rigidly cross-linked ($k = 5$ pN/nm), tightly spaced ($s = 0$ nm) F-actin bundle. At this rigidity and spacing, the deformation of the F-actin springs and cross-linkers is negligible, resulting in an effectively rigid bundle. For $p = 1$, a completely unipolar bundle that corresponds to the experimental fascin-bundled F-actin, the myosin travels micrometers over a period of seconds in one direction, toward the F-actin barbed ends, consistent with experiments (Fig. 3 B). As p decreases, the total myosin filament displacement also decreases, and the corresponding decreased velocity reflects an increasing resistance from motor binding to F-actin with opposing orientation. When $p = 0.5$, myosin filaments move only a few nanometers, similar to the confined motion we experimentally observe on mixed-polarity bundles.

With this simulation, we can interrogate how the instantaneous force exerted by a myosin filament depends on the F-

actin bundle polarity. We find the force generated on bundles with the most uniform polarity is lowest (Fig. 3 C, red x symbols), whereas the force exerted on bundles with mixed polarity is highest (Fig. 3 C, blue x symbols). Inspection of the forces exerted by the myosin filament on individual F-actin reveals that myosin binding to opposing F-actin in the bundle, N_- , resist the myosin movement on F-actin oriented in the positive direction, resulting in the buildup of a force dipole. When the forces in the positive direction are not fully balanced by those in the opposing direction, processive motor motion in the positive direction occurs. This indicates that the forces a myosin filament exerts on the F-actin oriented in the positive direction, N_+ , are effectively determined by the motor interactions with F-actin of opposing polarity, N_- . By plotting the average force and average myosin velocity measurements of bundles over a range of polarities, we see that these fall on a curve consistent with the known force-velocity relationship of myosin II, which is encoded by the model (Fig. 3 C, black lines; (29)). The range of forces for each polarity reflect the stochasticity of the system and fluctuations in number of binding interactions. As the polarity becomes more mixed, the force approaches a maximum, determined by the stall force of each motor head and by the total number of motor interactions with F-actin. Consequently, reducing the number of F-actin in the bundle to five results in a similar force-velocity relationship but with nearly half of the maximal force generated in a bundle with 20 F-actin (Fig. 3 C, circles).

Although experimental control of the myosin filament size (N_{heads}) or the number of F-actin within a bundle is complex, we can vary the number of motor heads in simulations to gain further insight into the microscope mechanisms of force

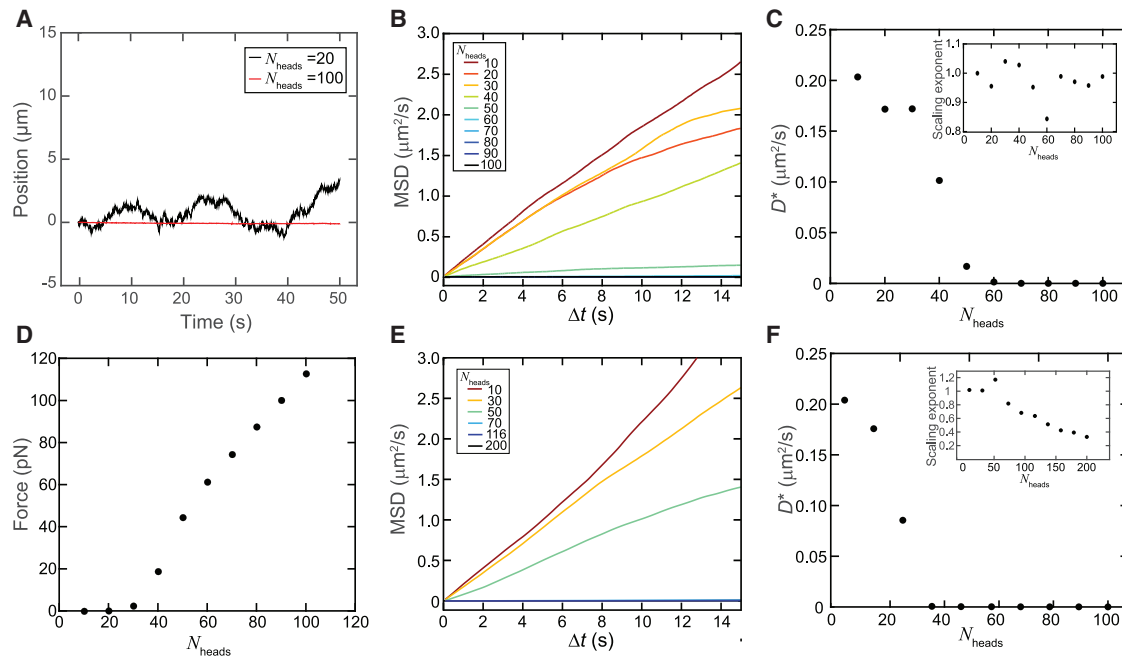


FIGURE 4 Number of myosin heads influences myosin dynamics and force generation. (A) Trajectories on $s = 10$, $p = 0.5$ bundles for $N_{\text{heads}} = 20$ and $N_{\text{heads}} = 250$. (B) Myosin filament mean-square displacement as a function of delay time for bundles with $p = 0.5$, $s = 10$ nm, and $k = 10$ pN/nm. (C) Myosin filament diffusion quantified by D^* , which is proportional to the generalized diffusion coefficient, as a function of the number of heads. D^* is extracted from a fit to the data in (C), $MSD = D^*e^{\beta}$. Inset is the scaling exponent, β as a function of the N_{heads} . (D) Force as a function of the number of myosin heads for myosin on a 10 nm spaced bundle, $N_+ = N_- = 3$ with rigid cross-links ($k = 10$ pN/nm). (E) Myosin filament mean-square displacement as a function of delay time for bundles with $p = 0.5$, $s = 10$ nm, and $k = 0.02$ pN/nm. (F) Similar to (C), D^* and β (inset) extracted from fitting the mean-square displacement in (E) to $MSD = D^*e^{\beta}$. To see this figure in color, go online.

production. For mixed-polarity bundles ($p = 0.5$, $N_+ = 3$), myosin filaments with $N_{\text{heads}} < 40$ have short runs with frequent direction switching (Fig. 4 A, black). From the mean-square displacement as a function of delay time, we find a scaling exponent near one, indicating that the myosin filament motion is effectively diffusive, with an effective diffusion coefficient $\sim 0.1\text{--}0.2 \mu\text{m}^2/\text{s}$ (Fig. 4, B and C). This is consistent with dynamics that arise from stochastic effects, with significant force imbalances leading to large displacements (29,45). As N_{heads} increases >40 , the myosin movement is reduced (Fig. 4 A, red). The motion remains diffusive, but the diffusion coefficient decreases to nearly zero (Fig. 4, B and C). Thus, for $p = 0.5$, the myosin filament motion is diffusive over all N_{heads} , but the diffusion constant decreases with increasing N_{heads} (Fig. 4 C; (46)). Above a critical value of N_{heads} , the force—which is the product of N_{heads} and the duty ratio, or the fraction of time that individual motors spend bound to F-actin (29)—increases proportionally with N_{heads} (Fig. 4 D). In cells, different isoforms of myosin II form filaments composed of multiple motor heads, ranging from several to several hundred motor heads. In our previous study, the mean value of N_{heads} under similar experimental conditions was ~ 250 (47). These data suggest that as the number of heads increases, the probability of at least one bound motor engaging to F-actin of both polarities increases, a prerequisite to building force. As this probability increases, the overall diffusivity of the motor on the mixed-polarity bundle decreases, resulting

in minimal displacement and maximal force build up. Together, these data highlight the impact of the number of motor heads in the potential of collections of motors to generate forces.

To examine whether cross-linker flexibility influences myosin trapping, we examine the MSD with a lower value of $k = 0.02$ pN/nm. Similar to the rigid cross-linker simulations, the MSD decreases with increasing N_{heads} . For small values of N_{heads} (50 or less), the MSD is larger at the lower stiffness. However, for $N_{\text{heads}} \geq 70$, the myosin filaments are similarly highly trapped as at the higher stiffness. Intriguingly, the scaling exponent for the MSD becomes subdiffusive with increasing N_{heads} for compliant bundles. The effective diffusion coefficient similarly decreases with N_{heads} as in the rigid bundles. These simulations predict that motion of myosin filaments with a small range of N_{heads} will be responsive to cross-linker stiffness but that myosin filaments in our experimental assay ($N_{\text{heads}} \sim 250$ (47)) would be highly trapped with increased cross-linker flexibility at low filament spacing.

Myosin trapping is abrogated on filamin bundles and robust on α -actinin bundles

In addition to F-actin polarity, both the interfilament spacing and bundle compliance can be experimentally varied when constructing F-actin bundles with different cross-linkers.

We hypothesize that changing the interfilament spacing potentially impacts the number of accessible F-actin binding sites for a motor complex bound to a bundle, whereas changes in the local bundle compliance could influence the force-dependent motor binding affinity (29,46). Thus, we expect that the interfilament spacing and bundle compliance affect the number of motor heads bound, impacting the force generation potential of a given bundle architecture.

To investigate this, we experimentally constructed bundles formed with the cross-linkers α -actinin and filamin. These cross-linkers form mixed-polarity bundles, similar to fimbrin, but form bundles with different interfilament spacing and compliance (4,10,48,49). Cross-linking with α -actinin forms bundles with ~ 35 nm interfilament spacing (Fig. 5, A and B*i*; (48)). Projections of myosin intensity on α -actinin cross-linked bundles over a 5 min period appear as dense tracks along micron-sized regions of bundles (Fig. 5 C*i*). Despite different spacing, kymographs reveal regions of bidirectional motion and pauses, indicating myosin has similar motion as it does on fimbrin cross-linked bundles (Fig. 5 D*i*). Over 217 individual myosin tracks, $\sim 60\%$ of myosin move intermittently, similar to what we observe on fimbrin bundles (Fig. 5 F, *solid blue line* and *solid blue circles*). However, in contrast to fimbrin bundles, on α -actinin cross-linked bundles, myosin are only continuously confined to a trap over a 5 min period in $\sim 8\%$ of the tracks, whereas they continuously move in $\sim 35\%$ of the cases (Fig. 5 E, *blue*).

To increase the interfilament spacing, we construct bundles using the cross-linker filamin, which has arms linked by disordered protein regions that result in a flexible hinge-like structure (Fig. 5, A and B*ii*; (4,49)). Bundles constructed from F-actin cross-linked by 5 mol% filamin are loosely spaced collections of F-actin. In contrast to the smaller-spaced bundles, projections of myosin over a 5 min period form tracks spanning several microns of filamin cross-linked bundles (Fig. 5 C*ii*, *white*). Kymographs along filamin cross-linked bundles reveals markedly different myosin behavior, in which tracks appear as zig-zagging lines, indicating direction switching over multiple length scales (Fig. 5 D*ii*). Notably, in contrast to the other mixed-polarity bundles, kymographs of myosin motion on filamin bundles contain no vertical lines of measurable duration, indicating that filamin bundles support continuous motion without confinement, with instantaneous velocity up to ~ 500 nm/s (Fig. 5 F, *black dashed line* and *solid black circles*). Intriguingly, increasing the number of filamin cross-links in a bundle to 25 mol% restores myosin motion to the motion characteristic of smaller-spaced mixed-polarity bundles (Fig. 4, B*iii* and C*iii*), in which periods of motion are interspersed with traps (Fig. 5 D*iii*). The distribution of myosin that move continuously, intermittently, and are confined is similar to myosin on fimbrin bundles (Figs. 2 F, *black* and 5 E, *gray*). In the regions of motion, myosin on high filamin bundles has a speed of ~ 300 nm/s, consistent with myosin movements on fimbrin cross-linked actin (Fig. 5 F, *open gray circles*).

Bundle spacing and compliance influence myosin trapping and force generation

To systematically investigate the influence of bundle spacing on myosin activity, we simulated a myosin filament on a mixed-polarity bundle ($p = 0.5$, $N_+ = N_- = 3$, $k = 10$ pN/nm) with variable interfilament spacing. Similar to our experimental observations, we find that myosin filaments with $N_{\text{heads}} = 200$ are trapped in sustained pauses at the smallest spacing, $s = 10$, but switch between intermittent runs and confined traps at the largest spacing, $s = 200$ nm (Fig. 6 A).

To understand the impact of bundle spacing on forces generated by myosin, we quantified average force as a function of N_{heads} . On a tightly spaced bundle, the force is near zero below a critical value (~ 10 heads) and then increases linearly with increasing N_{heads} (Fig. 6 B, *blue*), consistent with previous reports of myosin motors on individual F-actin (29). At or above the critical N_{heads} value, the force-dependent increase in the bound lifetime of myosin heads results in a positive feedback between force generation and myosin attachment (29). Below the critical number of myosin heads bound, the entire myosin filament frequently detaches, resulting in force relaxation, whereas above it, the myosin filament remains bound for long times (29). The critical N_{heads} to transition to increasing force increases with s , whereas the slope of the force dependence on N_{heads} decreases with s (Fig. 6 B). The dependence of the force- N_{heads} relationship on interfilament spacing suggests that different spacings can support different force outputs for myosin with the same value of N_{heads} .

In addition to differences in cross-linker size, which controls interfilament spacing, cross-linkers such as filamin and α -actinin differ in stiffness, which controls the bundle's mechanical compliance. Decreasing the stiffness of the elastic load on which myosin motors build force decreases the total force output (29,46,50–52). This occurs because decreasing the stiffness reduces the rate of force buildup and reduces the positive feedback between myosin attachment time and force buildup (29,46). Indeed, we find that for bundles with large spacing ($s = 200$, $p = 0.5$, $N_+ = N_- = 3$) the motion exhibits complex behavior as a function of cross-linker stiffness (Fig. 6 C). The myosin filaments are the most motile at the lowest value of stiffness, $k = 0.02$ pN/nm. This arises both from longer runs of the myosin filament in a given direction as well as differences in the nature of the trapped regions. At $k = 0.02$ pN/nm, there are larger position fluctuations in regions of the trajectory where the myosin filament is relatively trapped (e.g., Fig. 6 C, *black curve*, 35–45 s) as compared to trapped regions at higher k in Fig. 6 C. For a given N_{heads} , the average force increases with increasing stiffness, whereas the critical N_{heads} for myosin to exert a nonzero force increases with decreasing stiffness (Fig. 6 D). Together, these data suggest that differences in both

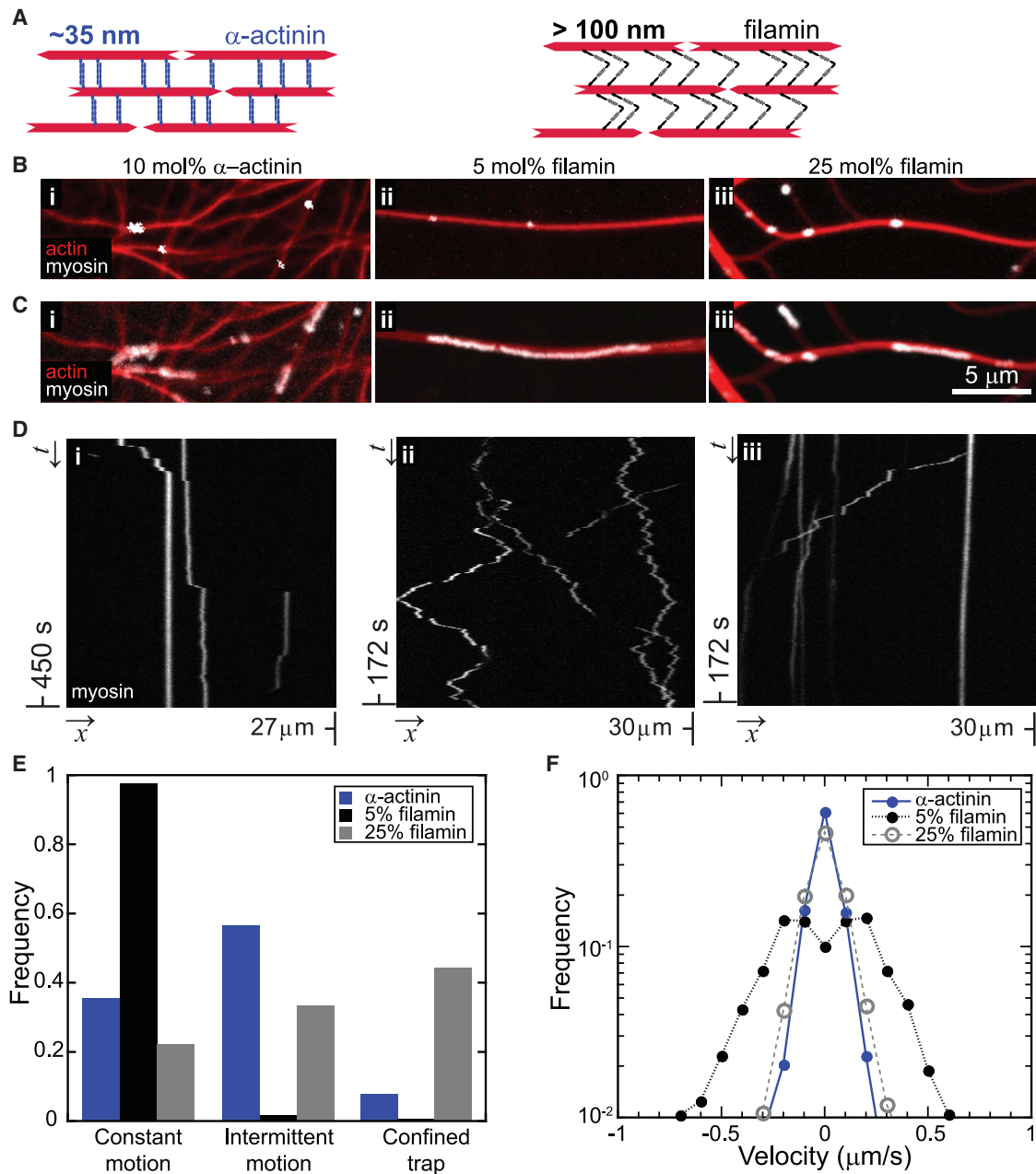


FIGURE 5 Bundle spacing and stiffness regulate myosin dynamics. (A) Cartoon of mixed-polarity bundles constructed by the ~ 35 nm rigid cross-linker, α -actinin, and the ~ 150 nm hinged cross-linker, filamin. (B) Bundles of F-actin (red) cross-linked by 10 mol% α -actinin (left), 5 mol% filamin (middle), and 25 mol% filamin (right) with isolated myosin II motors (white puncta). (C) Maximal intensity projection of myosin II on the bundles, showing that myosin II explores space on 5 mol% filamin bundles (middle), but on 10 mol% α -actinin (left) and 25 mol% filamin (right), bundles appear in localized, micron-sized regions of the bundles (right). (D) Representative kymographs of myosin along different cross-linked bundles. 5 mol% filamin bundles (middle) show zig-zag diagonal lines with no vertical lines, indicating constant motion in the form of short runs in one direction, followed by runs in the opposite direction. Myosin II on 10 mol% α -actinin (left) and 25 mol% filamin (right) bundles appears as long vertical lines interspersed with short, diagonal lines (middle), indicating motion dominated by trapping similar to fimbrin. (E) Summary of the frequency of myosin dynamics—intermittent motion and pauses, constant motion, or sustained pauses—from kymographs represented in (E) (α -actinin: 217, 5 mol% filamin: 167, 25 mol% filamin: 275 myosin). (F) Velocity distributions for the different cross-linked bundles are all symmetric about zero, indicating bidirectional motion. 5 mol% filamin (black dashed line and solid circles) has a minimum at zero, indicating little trapping and average nonzero speed ~ 300 nm/s, whereas 10 mol% α -actinin (blue solid line and circles) and 25 mol% filamin (gray dashed line and open circles) have maxima at zero, indicating increased trapping. To see this figure in color, go online.

length and flexibility account for the lower forces produced by myosin on bundles formed by filamin, as flexibility alone has small effects on the MSD in Fig. 4.

We note that for a given force output, myosin trajectories vary as a function of bundle spacing or stiffness, making direct inference of forces from these dynamics challenging.

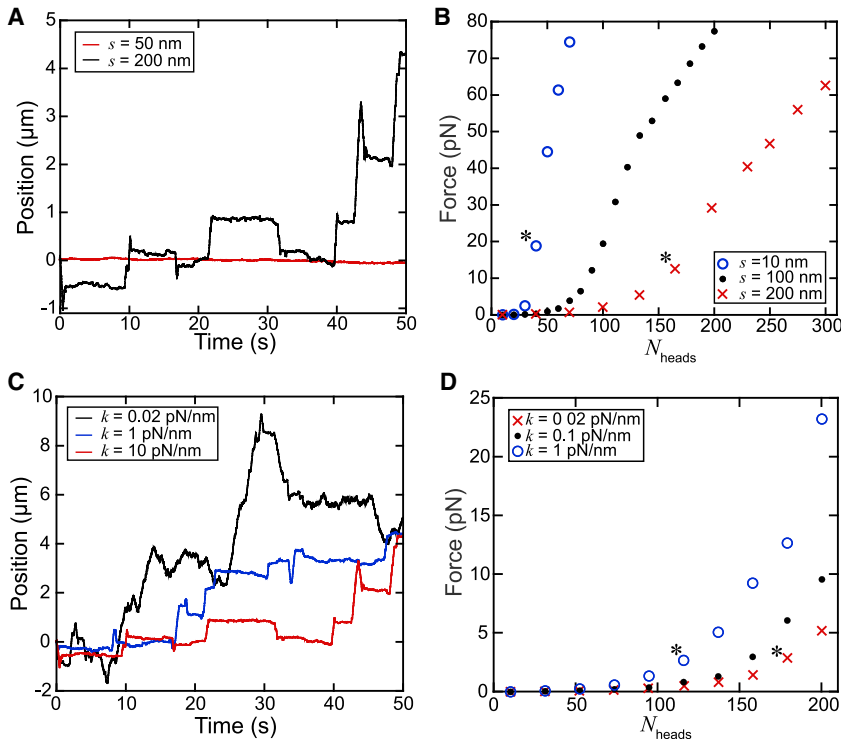


FIGURE 6 Forces exerted by myosin filaments at varying F-actin spacing cannot be readily inferred from velocity or distance traveled. (A) Trajectories on a bundle with $p = 0.5$, $k = 10$ pN/nm, $N_{\text{heads}} = 200$, and spacing $s = 50$ and 200 nm. (B) The number of motor domains, N_{heads} , and spacing, s , affect the time-averaged force, F . At increasing s , indicated by darker gray, the transition to nonzero force production with increased N_{heads} is less steep. Value of k is 10 pN/nm. Asterisks indicate data in (D). (C) Myosin filaments transition from weak attachment and noisy trajectories at low stiffness to tight trapping with increased stiffness. Representative trajectories at $s = 200$ nm, $N_{\text{heads}} = 200$ are shown. (D) Force output as a function of N_{heads} , for different stiffness bundles with $s = 200$ nm. Asterisks indicate data in (B). To see this figure in color, go online.

For stiff bundles ($k = 10$ pN/nm, $F = 15$ – 20 pN), corresponding to asterisks in Fig. 6 B, myosin are completely trapped at the smallest spacing ($s = 10$ nm, Fig. 7 A, red) but exhibit intermittent motion at the largest spacing (Fig. 7 A, black). Similarly, we find that myosin with similar force outputs are characterized by very different motilities for bundles of different stiffness (Fig. 6 B, corresponding to 6 D, asterisks). For large spacing ($s = 200$ nm), myosin are relatively trapped with intermittent short runs at extreme stiffnesses (Fig. 7 B, black, $k = 1$ pN/nm) but move in long runs frequented by direction switching at intermediate stiffness (Fig. 7 B, red, $k = 0.02$ pN/nm).

Trap strength is directly related to the average generated force

To extract information about myosin-generated forces from myosin trajectories, we detect traps by plotting the probability that a myosin filament is located in a specific position along the bundle during each 50 s simulation and find local peaks in the probability distribution. We define the height of each peak as the trap strength. We average the trap strength, as well as the force, during 10 independent 50 s simulations using systematically varied parameter values of N_{heads} , bundle spacing, and cross-link stiffness (Fig. 7 C). The average trap strength is highly variable with respect to the average force, with different bundle architectures dominating different regions of the pause space (Fig. 7 C; e.g., blue triangles: $k = 10$ pN/nm, $p = 0.5$, $s = 10$ nm; red x symbols: $k = 10$ pN/nm, $s = 200$ nm, $p = 0.5$; orange circles:

$k = 10$ pN/nm, $s = 10$ nm, $p = 0.6$; each data point is for trajectories with one value of N_{heads}). This variability is consistent with sensitive dependence of myosin force generation on the microscopic bundle architecture and motor binding affinity.

To further distinguish between high-force and low-force signatures in trajectories, we consider the trajectory straightness, defined as the ratio between the final displacement and the pathlength. Transient traps with small durations can occur either because the myosin is mostly unbound to actin or because the myosin is able to bind but is continually walking in a direction determined by the polarity of its interactions with F-actin. In the former scenario, the force is very small because of the transient nature of the binding interactions; in the latter scenario, the force is variable and determined by the force-velocity relationship of the motors. These two situations can be distinguished from one another by plotting the strength of an individual trap against the trajectory straightness within a trap (Fig. 7 D). Transient, low-force interactions such as those occurring at small N_{heads} ($N_{\text{heads}} = 20$, $s = 10$ nm $N_+ = N_- = 3$; Fig. 7 D, region II) have relatively small values of both trap strength and trajectory straightness. On the other hand, myosin filaments that interact more strongly with the local F-actin but do so in a polar fashion display small values of trap strength but high values of straightness ($N_{\text{heads}} = 200$, $s = 200$ nm $N_+ = N_- = 3$; Fig. 7 D, region I). Traps with long durations that are highly force-generating have small values of local trajectory straightness ($N_{\text{heads}} = 100$, $s = 10$ nm $N_+ = N_- = 3$; Fig. 7 D, region III). Using this metric to

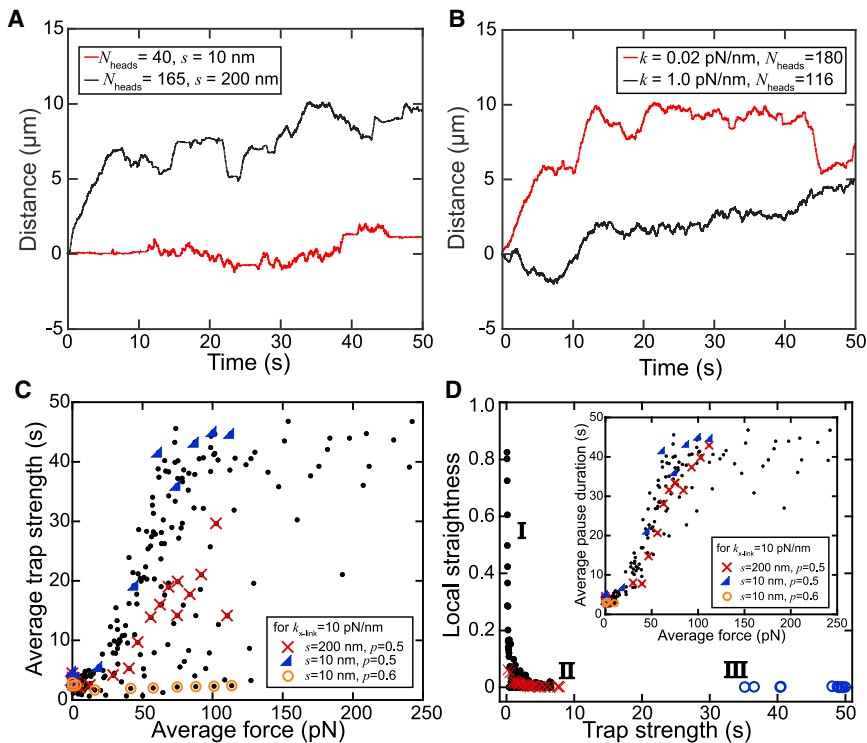


FIGURE 7 Pause time and trajectory straightness reveal qualitative differences in force generation. (A) Trajectories for myosin on bundles with different spacing, $s = 10 \text{ nm}$ (red, $N_{\text{heads}} = 40$) and $s = 200 \text{ nm}$ (black, $N_{\text{heads}} = 165$) at the same force output exhibit different motility characteristics. Force corresponds to data points from blue open circle and red x curves in Fig. 6 B. (B) Trajectories for myosin at the same force output on different stiffness, $k = 0.02 \text{ pN/nm}$ (red, $N_{\text{heads}} = 180$) and $k = 1 \text{ pN/nm}$ (black, $N_{\text{heads}} = 116$); bundles exhibit different motility characteristics. Force corresponds to asterisks in Fig. 6 B. (C) The average trap strength, defined as the height of peaks in the distribution of myosin position, plotted against average force for each set of parameters in Figs. 3, 4, and 6 including all values of N_{heads} , s , k , and p . Highlighted examples are rigid bundles with small spacing ($k = 10 \text{ pN/nm}$, $s = 10 \text{ nm}$, $p = 0.5$, blue triangles), rigid bundles with larger spacing ($k = 10 \text{ pN/nm}$, $s = 200 \text{ nm}$, $p = 0.5$, red x symbols), and rigid polar bundles ($k = 10 \text{ pN/nm}$, $s = 10 \text{ nm}$, $p = 0.6$, orange circles). (D) Trap strength for each peak in the myosin position histogram against the local straightness. In region I, the trap strength is small because the myosin is continually moving on a straight trajectory. Myosin binds with high affinity but exerts variable forces in this regime with unloaded speeds indicating a lack of force production. In region II, the trap strength is small because myosin is weakly attached and diffuses. In region III, myosin is tightly trapped because it binds with high affinity to an apolar region and produces high forces. Data are from simulations with small actin spacing and stiff cross-linkers ($s = 10 \text{ nm}$, $k = 10 \text{ pN/nm}$) and $N_{\text{heads}} = 20$ (red x symbols) or $N_{\text{heads}} = 100$ (blue circles). The black circles indicate data points corresponding to the trajectory in Fig. 6 A (red) ($N_{\text{heads}} = 200$, $s = 200$, $k = 10 \text{ pN/nm}$). (D, inset) Average trap strength is quantified only for peaks in the myosin position distribution where the straightness parameter of the local myosin filament trajectory is less than 0.1. When regions of locally straight myosin motion are excluded from the pause duration analysis in (C), the data collapse to a single curve. To see this figure in color, go online.

differentiate between different traps, we discard traps with highly variable forces where the myosin filament moves with a straightness parameter > 0.1 and find that the average force is directly proportional to pause duration for forces $< 100 \text{ pN}$ (Fig. 7 D, inset). This indicates that myosin in weak traps produce little or no forces, whereas myosin in strong traps generate large forces.

DISCUSSION

Cells have a myriad of cytoskeletal architectures that mediate physiological processes as diverse as directing transport to supporting cellular shape change. Here, we find that diverse F-actin bundle architectures constructed from physiological cross-linkers support different dynamics of myosin II complexes. Bundle architecture has been shown to influence protein segregation (53). Steric considerations such as interfilament spacing can influence protein binding, as has been shown for cross-linker binding (10,11). Similarly, filament polarity and interfilament spacing within bundles have been shown to influence motor transport in vitro (16,40,54). Regional differences in bundle architecture have been shown to influence the localization of proteins, such as different myosin isoforms, to different areas of the cell (17,55). Future research might explore

the further contributions of differences in interfilament angle, such as those observed in branched actin networks assembled by ARP 2/3.

Although architecture has been hypothesized to regulate protein segregation and cellular transport because of motor preference, the effects of architecture on cellular force generation is a nascent field. Mixed-polarity architecture in bundles has been shown to promote contractility (56), and the deformations depend on actin bundling (20). Here, we relate the experimentally observed motor dynamics to force generation through agent-based simulations. Our research has focused on filaments of skeletal muscle myosin II, which forms larger motor complexes than the isoforms of myosin II found in nonmuscle cells. Because our simulations suggest that the force generation potential depends sensitively on the number of motor heads in a complex, it would be interesting to explore how different isoforms of myosin II respond to different actin architectures.

Our results have implications for how force generation may be spatially regulated in the cell through bundle mechanics. Intriguingly, we show that compliant, filamin cross-linked bundles can be tuned, switching from negligible force production (loose traps) to tight traps or runs with increased cross-linker stiffness. Cross-linkers and other F-actin binding proteins could potentially dynamically tune

local bundle mechanics, leading to spatial and temporal control of force generation. The different dependencies of myosin isoforms on mechanical feedback in building force (29,57) might cause bundle mechanics to shape the force response to different isoforms. We hypothesize that the isoform nonmuscle myosin IIa will be the most sensitive to bundle mechanics because of its force building mechanism (29,57). These and other isoform-specific properties may play a role in differential localization of nonmuscle myosin II isoforms observed within cells (58). Together, this work presents a framework for the analysis of force generation in cytoskeletal networks inside and outside of cells. Additionally, understanding the effects of microstructure on force generation has the potential to inform the design of artificial active polymeric materials with tunable force response.

ACKNOWLEDGMENTS

We thank members of the David Kovar Laboratory for purified protein cross-linkers, particularly J. Winkelman, C. Suarez, J. Christensen, and Y. Li.

This research was partially supported by the University of Chicago Materials Research Science and Engineering Center, funded through the National Science Foundation award DMR-1420709. This research was funded by the National Science Foundation grants DMR-1905675 to M.L.G., the National Institute of General Medical Sciences grant R01GM098441 to E.M., and the National Institutes of Health National Institute of Biomedical Imaging and Bioengineering Training grant number T32EB009412 (S.S.).

REFERENCES

- Levayer, R., and T. Lecuit. 2012. Biomechanical regulation of contractility: spatial control and dynamics. *Trends Cell Biol.* 22:61–81.
- Blanchoin, L., R. Boujmaa-Paterski, ..., J. Plastino. 2014. Actin dynamics, architecture, and mechanics in cell motility. *Physiol. Rev.* 94:235–263.
- Agarwal, P., and R. Zaidel-Bar. 2019. Principles of actomyosin regulation in vivo. *Trends Cell Biol.* 29:150–163.
- Nakamura, F., T. P. Stossel, and J. H. Hartwig. 2011. The filamins: organizers of cell structure and function. *Cell Adhes. Migr.* 5:160–169.
- Foley, K. S., and P. W. Young. 2014. The non-muscle functions of actinins: an update. *Biochem. J.* 459:1–13.
- Bartles, J. R. 2000. Parallel actin bundles and their multiple actin-bundling proteins. *Curr. Opin. Cell Biol.* 12:72–78.
- Murrell, M., P. W. Oakes, ..., M. L. Gardel. 2015. Forcing cells into shape: the mechanics of actomyosin contractility. *Nat. Rev. Mol. Cell Biol.* 16:486–498.
- Huxley, A. F. 1957. Muscle structure and theories of contraction. *Prog. Biophys. Biophys. Chem.* 7:255–318.
- Huxley, A. F. 1974. Muscular contraction. *J. Physiol.* 243:1–43.
- Winkelman, J. D., C. Suarez, ..., D. R. Kovar. 2016. Fascin- and α -actinin-bundled networks contain intrinsic structural features that drive protein sorting. *Curr. Biol.* 26:2697–2706.
- Freedman, S. L., C. Suarez, ..., G. M. Hocky. 2019. Mechanical and kinetic factors drive sorting of F-actin cross-linkers on bundles. *Proc. Natl. Acad. Sci. USA.* 116:16192–16197.
- Scholz, M., K. L. Weirich, ..., A. R. Dinner. 2020. Tuning molecular motor transport through cytoskeletal filament network organization. *Soft Matter.* 16:2135–2140.
- Ando, D., N. Korabel, ..., A. Gopinathan. 2015. Cytoskeletal network morphology regulates intracellular transport dynamics. *Biophys. J.* 109:1574–1582.
- Kerber, M. L., D. T. Jacobs, ..., R. E. Cheney. 2009. A novel form of motility in filopodia revealed by imaging myosin-X at the single-molecule level. *Curr. Biol.* 19:967–973.
- Nagy, S., B. L. Ricca, ..., R. S. Rock. 2008. A myosin motor that selects bundled actin for motility. *Proc. Natl. Acad. Sci. USA.* 105:9616–9620.
- Conway, L., M. W. Gramlich, ..., J. L. Ross. 2014. Microtubule orientation and spacing within bundles is critical for long-range kinesin-1 motility. *Cytoskeleton (Hoboken).* 71:595–610.
- Pfisterer, K., J. Levitt, ..., M. Parsons. 2020. FMNL2 regulates dynamics of fascin in filopodia. *J. Cell Biol.* 219:e201906111.
- Koenderink, G. H., and E. K. Paluch. 2018. Architecture shapes contractility in actomyosin networks. *Curr. Opin. Cell Biol.* 50:79–85.
- Ennomani, H., G. Letort, ..., L. Blanchoin. 2016. Architecture and connectivity govern actin network contractility. *Curr. Biol.* 26:616–626.
- Stam, S., S. L. Freedman, ..., M. L. Gardel. 2017. Filament rigidity and connectivity tune the deformation modes of active biopolymer networks. *Proc. Natl. Acad. Sci. USA.* 114:E10037–E10045.
- Spudich, J. A., and S. Watt. 1971. The regulation of rabbit skeletal muscle contraction. I. Biochemical studies of the interaction of the tropomyosin-troponin complex with actin and the proteolytic fragments of myosin. *J. Biol. Chem.* 246:4866–4871.
- Vignjevic, D., S. Kojima, ..., G. G. Borisy. 2006. Role of fascin in filopodial protrusion. *J. Cell Biol.* 174:863–875.
- Skau, C. T., and D. R. Kovar. 2010. Fimbrin and tropomyosin competition regulates endocytosis and cytokinesis kinetics in fission yeast. *Curr. Biol.* 20:1415–1422.
- Li, Y., J. R. Christensen, ..., D. R. Kovar. 2016. The F-actin bundler α -actinin Ain1 is tailored for ring assembly and constriction during cytokinesis in fission yeast. *Mol. Biol. Cell.* 27:1821–1833.
- Craig, S. W., C. L. Lancashire, and J. A. Cooper. 1982. Preparation of smooth muscle alpha-actinin. *Methods Enzymol.* 85:316–321.
- Margossian, S. S., and S. Lowey. 1982. Preparation of myosin and its subfragments from rabbit skeletal muscle. *Methods Enzymol.* 85:55–71.
- Verkhovsky, A. B., and G. G. Borisy. 1993. Non-sarcomeric mode of myosin II organization in the fibroblast lamellum. *J. Cell Biol.* 123:637–652.
- Danuser, G., and C. M. Waterman-Storer. 2006. Quantitative fluorescent speckle microscopy of cytoskeleton dynamics. *Annu. Rev. Biophys. Biomol. Struct.* 35:361–387.
- Stam, S., J. Alberts, ..., E. Munro. 2015. Isoforms confer characteristic force generation and mechanosensation by myosin II filaments. *Biophys. J.* 108:1997–2006.
- White, H. D., B. Belknap, and M. R. Webb. 1997. Kinetics of nucleoside triphosphate cleavage and phosphate release steps by associated rabbit skeletal actomyosin, measured using a novel fluorescent probe for phosphate. *Biochemistry.* 36:11828–11836.
- Trybus, K. M., and E. W. Taylor. 1982. Transient kinetics of adenosine 5'-diphosphate and adenosine 5'-(beta, gamma-imidotriphosphate) binding to subfragment 1 and actosubfragment 1. *Biochemistry.* 21:1284–1294.
- Guo, B., and W. H. Guilford. 2006. Mechanics of actomyosin bonds in different nucleotide states are tuned to muscle contraction. *Proc. Natl. Acad. Sci. USA.* 103:9844–9849.
- Veigel, C., J. E. Molloy, ..., J. Kendrick-Jones. 2003. Load-dependent kinetics of force production by smooth muscle myosin measured with optical tweezers. *Nat. Cell Biol.* 5:980–986.

34. Nakamura, F., T. M. Osborn, ..., T. P. Stossel. 2007. Structural basis of filamin A functions. *J. Cell Biol.* 179:1011–1025.
35. Chen, H., X. Zhu, ..., J. Yan. 2011. Differential mechanical stability of filamin A rod segments. *Biophys. J.* 101:1231–1237.
36. Mijailovich, S. M., O. Kayser-Herold, ..., M. A. Geeves. 2016. Three-dimensional stochastic model of actin-myosin binding in the sarcomere lattice. *J. Gen. Physiol.* 148:459–488.
37. Gillespie, D. T. 1976. A general method for numerically simulating the stochastic time evolution of coupled chemical reactions. *J. Comput. Phys.* 22:403–434.
38. Hill, A. V. 1938. The heat of shortening and the dynamic constants of muscle. *Proc. R. Soc. Lond. Ser. B. Biol. Sci.* 126:136–195.
39. Murrell, M., and M. L. Gardel. 2014. Actomyosin sliding is attenuated in contractile biomimetic cortices. *Mol. Biol. Cell.* 25:1845–1853.
40. Scholz, M., S. Burov, ..., A. R. Dinner. 2016. Cycling state that can lead to glassy dynamics in intracellular transport. *Phys. Rev. X.* 6:011037.
41. Ali, M. Y., S. B. Previs, ..., D. M. Warshaw. 2013. Myosin VI has a one track mind versus myosin Va when moving on actin bundles or at an intersection. *Traffic.* 14:70–81.
42. Spudich, J. A., S. J. Kron, and M. P. Sheetz. 1985. Movement of myosin-coated beads on oriented filaments reconstituted from purified actin. *Nature.* 315:584–586.
43. Kron, S. J., and J. A. Spudich. 1986. Fluorescent actin filaments move on myosin fixed to a glass surface. *Proc. Natl. Acad. Sci. USA.* 83:6272–6276.
44. Bretscher, A. 1981. Fimbrin is a cytoskeletal protein that crosslinks F-actin in vitro. *Proc. Natl. Acad. Sci. USA.* 78:6849–6853.
45. Erdmann, T., and U. S. Schwarz. 2012. Stochastic force generation by small ensembles of myosin II motors. *Phys. Rev. Lett.* 108:188101.
46. Albert, P. J., T. Erdmann, and U. S. Schwarz. 2014. Stochastic dynamics and mechanosensitivity of myosin II minifilaments. *New J. Phys.* 16:093019.
47. Thoresen, T., M. Lenz, and M. L. Gardel. 2013. Thick filament length and isoform composition determine self-organized contractile units in actomyosin bundles. *Biophys. J.* 104:655–665.
48. Pelletier, O., E. Pokidysheva, ..., C. R. Safinya. 2003. Structure of actin cross-linked with alpha-actinin: a network of bundles. *Phys. Rev. Lett.* 91:148102.
49. van der Flier, A., and A. Sonnenberg. 2001. Structural and functional aspects of filamins. *Biochim. Biophys. Acta.* 1538:99–117.
50. Mitrossilis, D., J. Fouchard, ..., A. Asnacios. 2009. Single-cell response to stiffness exhibits muscle-like behavior. *Proc. Natl. Acad. Sci. USA.* 106:18243–18248.
51. Borau, C., T. Kim, ..., R. D. Kamm. 2012. Dynamic mechanisms of cell rigidity sensing: insights from a computational model of actomyosin networks. *PLoS One.* 7:e49174.
52. Walcott, S., and S. X. Sun. 2010. A mechanical model of actin stress fiber formation and substrate elasticity sensing in adherent cells. *Proc. Natl. Acad. Sci. USA.* 107:7757–7762.
53. Michelot, A., and D. G. Drubin. 2011. Building distinct actin filament networks in a common cytoplasm. *Curr. Biol.* 21:R560–R569.
54. Ali, M. Y., A. Vilfan, ..., D. M. Warshaw. 2016. Cargo transport by two coupled myosin Va motors on actin filaments and bundles. *Biophys. J.* 111:2228–2240.
55. Brawley, C. M., and R. S. Rock. 2009. Unconventional myosin traffic in cells reveals a selective actin cytoskeleton. *Proc. Natl. Acad. Sci. USA.* 106:9685–9690.
56. Reymann, A.-C., R. Boujemaa-Paterski, ..., L. Blanchoin. 2012. Actin network architecture can determine myosin motor activity. *Science.* 336:1310–1314.
57. Melli, L., N. Billington, ..., J. R. Sellers. 2018. Bipolar filaments of human nonmuscle myosin 2-A and 2-B have distinct motile and mechanical properties. *eLife.* 7:e32871.
58. Maupin, P., C. L. Phillips, ..., T. D. Pollard. 1994. Differential localization of myosin-II isozymes in human cultured cells and blood cells. *J. Cell Sci.* 107:3077–3090.